Solution-Phase Synthesis of Alloyed Ba(Zr1-xTi$_x$)S$_3$ Perovskite and Non-Perovskite Nanomaterials

SCHOLARONE™
Manuscripts

ARTICLE

Solution-Phase Synthesis of Alloyed Ba(Zr$_{1-x}$Ti$_x$)S$_3$ Perovskite and Non-Perovskite Nanomaterials

Daniel Zilevu, Kennedi M. Miller, Naira Arrykova, Autumn B. Locke, Sidney E. Creutz*

Chalcogenide perovskites, especially BaZrS$_3$ and its related alloys, present a promising alternative to lead halide perovskites for optoelectronic applications due to their reduced toxicity and enhanced stability. However, the elevated temperature conditions necessary for preparing these materials create a barrier to their incorporation into thin-film devices. In this work, we report a solution-phase synthesis of colloidal nanoparticles of titanium-alloyed BaZrS$_3$, Ba(Zr$_{1-x}$Ti$_x$)S$_3$. The titanium alloying was achieved using reactive amide precursors in oleylamine solvent, and N,N'-diethylthiourea served as the sulfur source. Our methodology allowed for the synthesis of Ba(Zr$_{1-x}$Ti$_x$)S$_3$ nanomaterials at temperatures at or below 300 °C. The resulting nanocrystals exhibited a phase transition from an orthorhombic distorted perovskite structure to a hexagonal non-perovskite phase as the titanium content surpassed x = 0.11, accompanied by a morphological evolution from nanoplatelets to nanohexagons and ultimately nanobars. The UV-Vis-NIR absorption spectra of Ba(Zr$_{1-x}$Ti$_x$)S$_3$ nanoparticles exhibit increasing low-energy absorption as the titanium content is increased. This work contributes to the development of low-temperature synthesis methods for Ba(Zr$_{1-x}$Ti$_x$)S$_3$ nanomaterials, offering new potential pathways for materials design of chalcogenide perovskites for advanced optoelectronic applications.

Introduction

Organic-inorganic lead halide perovskite solar cells have attracted substantial attention in recent years, demonstrating a rapid escalation in power conversion efficiency (PCE) since their inception.[1–7] However, the long-term stability of perovskite materials such as CH$_3$NH$_3$PbI$_3$ remains a significant concern, despite significance progress in recent years;[8,9] their degradation is accelerated when exposed to ambient air, elevated temperatures, and electric fields.[10,11] The vulnerability of halide perovskites to these environmental factors is partly attributed to the ionic character and resulting lability of the metal-halogen bonds; a semiconductor material featuring more covalent bonding may have higher stability. Furthermore, the presence of the toxic element Pb presents an additional obstacle for the commercial viability of these materials.

In response to the challenges posed by the toxicity and stability concerns inherent in inorganic-organic lead halide perovskites, a class of ternary chalcogenide materials with the general formula ABQ$_3$, (A= Ca, Ba, Sr; B = Zr, Hf, Ti; Q= S Se) has been put forth as a promising alternative for optoelectronic and solar cell applications.[12,13] A subset of the materials in this class are known to take on a stable perovskite structure under at least some conditions, including CaZrS$_3$, SrZrS$_3$, BaZrS$_3$, CaHfS$_3$, and BaHfS$_3$;[13–15] of these, BaZrS$_3$ has garnered the most interest largely because of its lower observed band gaps, falling within the range of 1.75 to 1.94 eV.[12,14,16–21] While these values make it potentially competitive for solar cell applications, especially in a tandem device with silicon, these band gaps are somewhat higher than the ideal for single-junction solar cells and higher than those accessible with lead halide perovskites. However, theoretical calculations based on density functional theory (DFT) suggest that the band gap of BaZrS$_3$ can be reduced through alloying, either by incorporating 3d cation Ti^{4+} to lower the conduction band minimum (CBM) or by introducing 4p anion Se^{2-} to elevate the valence band maximum (VBM); both of these possibilities have been investigated experimentally as well as computationally.[14,22,23] However, it should be noted that neither BaTiS$_3$ or BaZrSe$_3$ is known to occur in a perovskite phase; BaTiS$_3$ crystallizes in a hexagonal ($P6_3/mmc$) phase consisting of one-dimensional chains of edge-sharing TiS$_6$ octahedra interspersed with Ba^{2+} cations.[13,24]

Syntheses of these materials, particularly BaZrS$_3$ and its titanium alloys, have historically relied on very high temperatures (≥ 900 °C), incompatible with typical thin-film device processing.[13,18,25,26] Improved synthetic approaches have recently allowed BaZrS$_3$ powder to be produced at temperatures as low as 550 °C, employing molten BaS$_3$ as a flux.[25,27,28] Some efforts have focused on preparing BaZrS$_3$ thin films; Surendran *et al*. achieved temperatures below 700 °C through pulsed laser deposition,[29] while Comparotto *et al*. grew

$^{a.}$ *Department of Chemistry, Mississippi State University, Mississippi State, MS 39759, United States of America*

BaZrS$_3$ thin films at 600 °C using sputtering and sulfurization.[30,31] More recently, significant advances have been made by Agarwal and Bart in preparing thin films from the solution deposition of molecular precursors, with crystalline thin films of BaZrS3$_3$, BaTiS$_3$, and BaHfS$_3$ produced at temperatures as low as 500 °C.[32,33]

An alternative approach to solution-processed thin film deposition is through the preparation and use of colloidal nanocrystal inks;[34,35] notably, Nag *et al.* have used a top-down approach to nanocrystal preparation and were able to apply the resulting materials in solution-processed field-effect transistor devices.[36] However, until recently, solution-phase syntheses of colloidal BaZrS$_3$ nanocrystals were unknown, possibly due in part to the difficulties associated with preparing chalcogenide compounds of highly oxophilic early transition metal cations.[37] We recently reported the successful solution-phase synthesis of BaZrS$_3$ nanoparticles from metal amide precursors within a temperature range from 275 °C to 365 °C.[38] Similar results were also reported by the Hages group, who used barium and zirconium dithiocarbamate precursors to produce BaZrS$_3$ nanoparticles through solvothermal decomposition in oleylamine at 350 °C.[39]

Theoretical insights from Meng *et al.* in a 2016 paper suggested that a titanium-doped BaZrS$_3$ material in an orthorhombic perovskite phase (Figure 1a) could serve as an effective light absorber for thin film solar cells with extremely thin absorber layers.[14] The absorption coefficients of Ba(Zr$_{1-x}$Ti$_x$)S$_3$ (x = 0.25, 0.5) were predicted to be higher than those of lead halide perovskites; however, their results also suggested that these alloys would likely be prone to decomposition into the corresponding ternary phases, especially for higher titanium contents, and they correspondingly reported unsuccessful attempts to prepare alloys with x = 0.1 and 0.2 through combination of binary sulfide precursors (BaS, TiS$_2$, and ZrS$_2$) at 800-1000 °C, which provided only a mixture of the ternary BaTiS$_3$ and BaZrS$_3$ materials.

A synthetic approach relying on sulfurization of Ba(Zr$_x$Ti$_{1-x}$)O$_3$—where solid solutions in the perovskite phase can be prepared throughout the compositional range[40]—has proven more successful in generating Ba(Zr$_{1-x}$Ti$_x$)S$_3$ alloys, albeit primarily at low levels of titanium incorporation. Reports of these alloys date back at least to 1988 when Okai *et al* attempted to prepare BaZr$_{1-x}$Ti$_x$S$_3$ alloys by sulfurization of oxide precursors with CS$_2$ at 800-1000 °C.[41] They found that the alloy with the composition Ba(Ti$_{0.75}$Zr$_{0.25}$)S$_3$ uniquely took on a tetragonal perovskite structure when further treated at high pressure and high temperature (1000 °C, 60 kbar), and could be isolated in this phase by quenching to room temperature before releasing the pressure. When prepared at normal atmospheric pressure, only mixtures of phases or hexagonal non-perovskite phases were formed. Limited experimental data was presented for these compounds and no optical characterization was provided.

More recent studies have focused on the synthesis of properties of Ba(Zr$_{1-x}$Ti$_x$)S$_3$ alloys that maintain a perovskite phase, as well as the optical characterization of the resulting materials. However, it has generally been found that perovskite-phase Ba(Zr$_{1-x}$Ti$_x$)S$_3$ materials are only readily accessible at compositions with x ≤ 0.05. For example, Nishigaki *et al.* prepared Ba(Zr$_{0.95}$Ti$_{0.05}$)S$_3$ by sulfurization of a polycrystalline oxide precursor at 1000 °C; the resulting material took on a perovskite *Pnma* structure isostructural to that of unalloyed BaZrS$_3$ with slightly decreased lattice parameters, and with no apparent impurity phases.[20] They reported a band gap of 1.63 eV and an Urbach energy of 70.8 meV for the alloy (compared to 1.95 eV and 28.1 meV, respectively, for BaZrS$_3$), as determined from ellipsometry measurements. Interestingly, the authors noted that they were unable to prepare the alloyed materials by direct combination of binary sulfide precursors, necessitating the use of the oxide sulfurization process instead. Furthermore, attempts to prepare an alloy with a higher titanium content (x = 0.1) resulted in phase segregation to produce BaTiS$_3$, similar to the observations of Meng *et al.*[14]

Work by Wei *et al* provided further details about the dependence of the optical and structural properties of Ba(Zr$_{1-x}$Ti$_x$)S$_3$ alloys on titanium content up to x = 0.04; they used a similar synthetic procedure involving sulfurization of oxide precursors at 1050 °C.[18] Samples with 1, 2, 3, and 4% titanium incorporation showed a systematic, nearly linear decrease in lattice parameter while maintaining an orthorhombic perovskite structure. However, titanium concentrations above 5% were observed to compromise the perovskite structure leading to impurity phases including BaS, TiS$_2$, ZrS$_2$ and BaTiS$_3$; no further shift in the crystallographic d-spacing of the alloyed material was observed. While the aforementioned results were all obtained on polycrystalline powders, the preparation of alloyed thin films has also been recently pursued; Sharma *et al.*[19] prepared alloyed oxide precursor thin films by spin-coating and annealing, followed by sulfurization with CS$_2$ in an attempt to prepare Ba(Zr$_{1-x}$Ti$_x$)S$_3$ alloy thin films with a titanium content up to 6%. However, an anomalous and unexplained increase of the apparent crystallographic d-spacing of the alloyed materials relative to unalloyed BaZrS$_3$—opposite of the expected and previously observed results—as well as the presence of large amounts of impurity phases (primarily BaTiS$_3$ and TiO$_2$) in all samples makes the true composition of these materials unclear.

Overall, these studies have confirmed theoretical predictions that incorporation of titanium has a dramatic effect on the bandgap of the Ba(Zr$_{1-x}$Ti$_x$)S$_3$ perovskites, even at low levels of alloying. However, work has largely been limited to x ≤ 0.05, and little characterization of materials with a wider range of titanium content is available; notably, recent studies have reported only phase segregation to give hexagonal BaTiS$_3$ for higher values of x, rather than the formation of alloyed hexagonal (non-perovskite) phase Ba(Zr$_{1-x}$Ti$_x$)S$_3$, although Okai's 1988 paper demonstrated that it is possible to form such a material.[41] Two other limitations of current studies are noteworthy: first, no successful direct synthesis (e.g., from binary and/or monoelemental precursors) of the alloys has yet been reported, only oxide sulfurization requiring temperatures of at least 1000 °C; and second, no unambiguous and clean formation of alloyed thin films has been reported, only

Nanoscale

ARTICLE

polycrystalline powders. Given these limitations, we were interested in investigating whether these alloys could be accessed from solution phase synthesis on a nanocrystal platform, which could open new avenues for synthetic investigation.

In this study, we report the successful synthesis of colloidal nanoparticles composed of Ti-alloyed $BaZrS_3$, $Ba(Zr_{1-x}Ti_x)S_3$, with x ranging from 0 to 0.59. The synthesis was achieved using reactive amide precursors in an oleylamine solvent at a temperature of 300 °C; N,N'-diethylthiourea served as the sulfur source, building upon methodologies previously employed in our studies of the synthesis of $BaTiS_3$ and $BaZrS_3$ nanomaterials.[38,42] The $Ba(Zr_{1-x}Ti_x)S_3$ nanomaterials exhibited a phase transition from an orthorhombic distorted perovskite crystal structure (Figure 1A) to a hexagonal non-perovskite phase (Figure 1B) when the measured titanium content reached 15%. This structural transition was concomitant with a morphological evolution, transitioning from the initial $BaZrS_3$ nanoplatelets to nanohexagons, and ultimately, to nanobars. We observed that alloyed nanoparticles in the hexagonal phase with measurable crystallinity begin to form at temperatures as low as 258 °C. As observed in bulk studies, incorporation of titanium shifts the apparent absorbance edge and increases the low-energy absorbance of the nanocrystals; at high titanium content (in the hexagonal phase) the absorbance in the near-IR increases, consistent with a low bandgap as measured for $BaTiS_3$.[43]

Methods

Materials and synthetic considerations

General. Tetrakis(dimethylamido)zirconium and -titanium ($Zr[N(CH_3)_2]_4$ and $Ti[N(CH_3)_2]_4$, 99.8%) were purchased from Sigma-
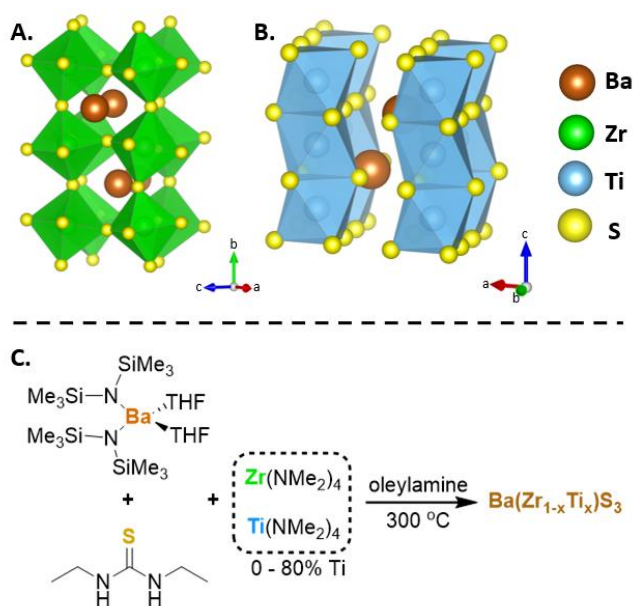

Figure 1. Structural depiction of Ti-alloyed $BaZrS_3$, showcasing (A) the orthorhombic distorted perovskite structure and (B) the non-perovskite hexagonal structure. Panel (C) presents the synthetic scheme employed for the synthesis of titanium-alloyed $BaZrS_3$ nanoparticles.

Aldrich and stored in an N_2 glovebox. $Zr[N(CH_3)_2]_4$ was further purified by sublimation before use. N,N'-Diethylthiourea, acquired from Alfa Aesar, was recrystallized from toluene and dried at 60 °C in vacuo overnight. Oleylamine (70%) from Sigma-Aldrich was refluxed at 120 °C over CaH_2, distilled *in vacuo*, transferred to an N_2 glovebox, filtered through activated alumina, and stored over 4 Å molecular sieves. For workups carried out in the glovebox, ethanol was dried by distilling from magnesium ethoxide, and degassed chloroform was dried by passing through activated alumina; both were stored over 4 Å molecular sieves. The barium precursor $Ba[N(SiMe_3)_2]_2(THF)_2$ was synthesized as described by Caulton *et al* with minor modifications as detailed in our previous work.[42,44]

Synthesis of $Ba(Zr_{1-x}Ti_x)S_3$ nanoparticles. We employed a heat-up approach, adapted from the protocol detailed in our previous research on $BaZrS_3$ nanoparticles.[38] In a glovebox, 1.7 g (2.46 mL) of anhydrous oleylamine was used to dissolve 90.8 mg (0.15 mmol) of $Ba[N(TMS)_2]_2(THF)_2$ in a 20 mL vial. This solution was then mixed with 53.8 mg (0.2 mmol) of $Zr[N(CH_3)_2]_4$ in a separate vial. Volumes ranging from 0 µl to 400 µL of a 0.404 M $Ti[N(CH_3)_2]_4$ solution in oleylamine were added to the Ba/Zr precursor solution. This combined mixture was subsequently transferred to a 25-mL Schlenk tube, which was equipped with a sidearm sealed by a Teflon valve and a Teflon-coated stir bar. Following this, 0.4 g (3 mmol) of solid N,N'-diethyl thiourea was added, and the resulting mixture was stirred for three minutes. Upon removing the flask from the glovebox, it was connected to an inert gas manifold and subjected to controlled heating at 300°C using a J-KEM PID temperature controller. This temperature was sustained for 30 minutes, after which the system was allowed to return to ambient conditions. For post-reaction procedures, the flask was reintroduced to the glovebox. To isolate the nanocrystals, the crude product was treated with approximately 5 mL each of ethanol and chloroform, followed by vigorous stirring. This mixture was then portioned into two test tubes and subjected to centrifugation at 2800 rpm. The supernatant was discarded, the precipitate underwent a subsequent wash with 5 mL of ethanol, and then it was redispersed in chloroform. The yield of the reaction was estimated to be approximately 52% (based on the mass of washed, dried nanocrystal precipitate) from a typical sample; however, this should be considered an upper limit of the true yield since the percent contribution of ligands to the sample mass was not explicitly determined.

The sample prepared with 80% nominal titanium content used 0.05 mmol of $Zr[N(CH_3)_2]_4$ and 0.2 mmol of $Ti[N(CH_3)_2]_4$, and otherwise followed the standard protocol described above.

Characterization

Powder X-ray diffraction (PXRD). For PXRD measurements, samples were prepared by drop-casting colloidal suspensions onto a zero-background silicon substrate. Data acquisition was conducted using an AXRD Benchtop diffractometer from Proto Manufacturing, employing Cu K_α radiation. This instrument featured a Dectris MYTHEN2 R 1D hybrid photon-counting detector and operated in Bragg-Brentano geometry.

Measurements were taken with a step size of 0.020°, employing dwell times ranging from 5 to 15 seconds and a 1 mm collimating slit. A measured background acquired on an empty substrate under the same conditions was subtracted from the data shown. Data refinement was carried out using GSAS-II.[45] Instrument calibration was achieved using a LaB_6 standard.

Transmission electron microscopy (TEM) and energy-dispersive X-ray spectroscopy (EDX) analysis. Samples intended for TEM observation were diluted in chloroform and sonicated. Subsequently, a droplet from this colloidal dispersion was placed on a carbon-coated copper TEM grid and allowed to dry. Prior to imaging, samples were stored overnight in a vacuum desiccator. All sample preparations were executed in a glovebox under nitrogen atmosphere. Imaging investigations were carried out using a JEOL 2100 TEM at an operating voltage of 200 kV. Elemental analysis was performed with an Oxford EDS system.

Elemental analysis by inductively coupled plasma mass spectrometry (ICP-MS) analysis. The Ti-alloyed $BaZrS_3$ samples were subjected to two successive washing and centrifugation steps using 5 mL of chloroform. After washing, nanocrystals were air-dried. Separate portions of each nanocrystal sample were subjected to two different digestion protocols. One portion was treated with an acid mixture of HNO_3, HCl, and HF (in a 3:1:1 ratio) and placed in a hot water bath for 2 hours; analysis of this sample was used to determine the Ti/Zr ratio. The second portion was treated with a 1:1 combination of HNO_3 and HCl acids followed by heating in a hot water bath for 2 hours; analysis of this sample was used to determine the Ba/Zr ratio. After digestion, the acidified samples were diluted to a 100 mL volume using ultrapure deionized water. Analyses were conducted on a Perkin Elmer ELAN DRC II instrument and compared to calibration curves derived from commercial Zr^{4+}, Ti^{4+}, and Ba^{2+} standards.

Safety Note: Hydrofluoric acid (HF) is highly corrosive and toxic. Proper safety measures, including specialized training and appropriate protective gear, are essential when handling HF. Immediate first-aid should be applied if any exposure occurs.[46]

UV−Vis−NIR. Samples intended for absorbance analysis were dispersed in a suitable solvent, either chloroform or tetrachloroethylene, through brief sonication. These samples were subsequently transferred to a quartz cuvette and measurements were conducted using a Perkin Elmer Lambda 900 spectrometer; data from a solvent blank is subtracted from the spectra shown.

Environmental stability tests. To qualitatively evaluate the sample stability under ambient conditions, the colloidal suspension was drop-cast on a zero-background silicon plate intended for PXRD analysis and left exposed to ambient air in the laboratory (average conditions in the laboratory during this period were approximately 20 °C and 40% relative humidity).

X-ray photoelectron spectroscopy. XPS studies were carried out using a PHI VersaProbe II instrument using a monochromated aluminum X-ray source at 1.4866 keV.

Computational methods. Calculations were carried out using the Quantum Espresso suite and the program PWSCF, version 7.2,[47,48] using the frozen-core projector augmented-wave (PAW) method with the PBESOL functional;[49,50] further detailed description of the methodology is provided in the Supporting Information.

Results and Discussion

Synthesis

Attempts to prepare multinary compounds present increasingly complex challenges as the number of constituents increases; targeting quaternary $Ba(Zr_{1-x}Ti_x)S_3$ materials requires balancing the reactivity of up to four different precursors, and finding conditions to favor the formation of the desired phase over possible binary or ternary phases. We have previously reported the solution-phase syntheses of $BaZrS_3$ and $BaTiS_3$ nanocrystals using metal amide precursors and N,N'-diethylthiourea in oleylamine; given the similar conditions used to access the ternary materials, we felt that it would likely be possible to combine these protocols to prepare alloyed materials. Here, we adapted our prior approach to target $Ba(Zr_xTi_{1-x})S_3$, using a heat-up protocol at a reaction temperature of 300 °C.[38,42] The use of highly soluble and reactive metal amide precursors facilitates the formation of the desired sulfide materials, but also necessitates the use of rigorously anhydrous conditions throughout the synthetic procedure; furthermore, the reaction benefits from a high concentration and significant excess of the sulfur precursor.[38,42] Briefly, the reactions were carried out by mixing $Ba[N(TMS)_2]_2(THF)_2$, $Zr[N(CH_3)_2]_4$, N,N'-diethylthiourea, and $Ti[N(CH_3)_2]_4$ in anhydrous oleylamine and then heating the mixture to 300 °C. Under standard conditions, the precursor ratio Ba:Zr:S was maintained at 1:1.3:20, while varying amounts of the titanium amide precursor added (ranging from 0 to 50% of the total B-site cation); for higher titanium contents (80% of total B-site cations), the amount of the zirconium precursor added was concomitantly decreased (see Experimental Section for further details). After 30 minutes, the crude product was cooled to room temperature, and the nanocrystals were washed with anhydrous ethanol and chloroform. It was observed that the resulting nanocrystals could be suspended in chloroform with sonication to form a well-dispersed colloid. In discussions below, the percentage of titanium precursor introduced relative to the total B-site cation precursor content in the reaction mixture is referred to as the "nominal" titanium content, while the actual titanium content of the isolated samples was measured by ICP-MS; unless otherwise stated, all titanium amounts (reported as *x* in $Ba(Zr_{1-x}Ti_x)S_3$) referred to in the discussion and figures below are the measured amounts.

Powder X-ray diffraction and structural characteristics

As noted in the introduction, BaZrS$_3$ crystallizes in a distorted orthorhombic perovskite structure (GdFeO$_3$-type, *Pnma*)[24,51,52] while BaTiS$_3$ takes on a non-perovskite hexagonal structure (BaNiO$_3$-type, *P*6$_3$/*mmc*) characterized by one-dimensional chains of face-sharing TiS$_6$ octahedra.[24] The inability of BaTiS$_3$ to form a stable perovskite is likely related to the small size of the Ti^{4+} ion, which results in its octahedral factor ($\mu = r_{Ti}/r_S$) being outside of the optimal range for perovskite formation.[13] Therefore, if a Ba(Zr$_{1-x}$Ti$_x$)S$_3$ alloy is accessible for all values of x, it is expected that a phase change from orthorhombic to hexagonal will occur at some point along the compositional range. Indeed, Okai *et al.* reported that for $x \geq 0.75$, bulk polycrystalline Ba(Zr$_{1-x}$Ti$_x$)S$_3$ takes on a BaNiO$_3$ structure type; however, intermediate compositions with $x \leq 0.75$ gave rise to mixtures in their report.[41]

Nanocrystals of unalloyed BaZrS$_3$ and BaTiS$_3$ have both been characterized by powder X-ray diffraction (PXRD) in prior work, and a few key observations about the structure and diffraction properties of the particles are reiterated here for context.[38,39,42] In the case of BaZrS$_3$, it was observed that the nanocrystals (depending on the reaction conditions) exhibited powder X-ray diffraction characteristics that were not completely consistent with the reported bulk *Pnma* structure, although analysis by X-ray total scattering and pair-distribution function (PDF) analysis suggested that the local structure was still perovskite-like.[38,39] The exact nature of the structural distortion that seems to occur on the nanoscale is not currently precisely known, due to the difficulty of structure determination on the nanoscale. Here, we use the *Pnma* structure (as reported by Lelieveld *et al*)[51] as an approximation for the BaZrS$_3$ and alloyed perovskite nanocrystals, while recognizing that this introduces some uncertainty in the structural analysis (Figure 2). In the case of BaTiS$_3$, it is known from the bulk literature that this material is in most cases better described as BaTiS$_y$ ($y \leq 3$) and is characterized by an incommensurate composite structure whose structural parameters and diffraction pattern depend strongly on the sulfur substoichiometry. In the nanocrystals,

this stoichiometry depends on the reaction conditions (including time and concentration) and is difficult to precisely control in practice. Typical values of y for the nanocrystals are approximately ~2.7 and above. This results in sample-to-sample variation of the structural parameters, which are most apparent in the length of the apparent crystallographic c unit cell axis; changes in the length of the a axis are much smaller but trend in the opposite direction from c.[38,52]

In Figure 2, the results of the powder X-ray diffraction analysis for Ba(Zr$_{1-x}$Ti$_x$)S$_3$ nanocrystals with different titanium alloying levels are presented, along with the volume per formula unit plotted against the titanium content measured using ICP-MS. The unit cell parameters were extracted from the PXRD data using LeBail refinement (see Supporting Information for details, Table S1 and Figures S3-S10); because of the change in space group, plotting the volume per formula unit provides a clearer picture of the alloying across the compositional range than the individual lattice parameters, and confirms a systematic decrease in volume as the smaller Ti^{4+} ions are incorporated across both phases. This trend is suggestive of successful alloying rather than the presence of mixtures of discrete BaTiS$_3$ and/or BaZrS$_3$ phases. As shown in Figure 2a, the X-ray diffraction patterns obtained for Ba(Zr$_{1-x}$Ti$_x$)S$_3$ nanocrystals with low levels of titanium alloying (x = 0, 0.09, 0.11) are qualitatively similar to those previously reported for unalloyed BaZrS$_3$ nanocrystals, which were assigned to a distorted perovskite structure.[53] LeBail refinement of the unit cell parameters (*Pnma*) and unit cell volume showed a small but systematic decrease in these parameters as titanium content increased from 0 to 11%. We attempted to fit the 11% alloy PXRD data to a hexagonal BaNiO$_3$ structure type as an alternative, but this consistently gave rise to higher R-values and implausible lattice parameters (e.g. $c = 4.9$ *vs*. the measured $c = 5.9$ for hexagonal BaTiS$_3$, see Figure S5). Therefore, we conclude that nanocrystals with a measured titanium content of up to 11% are structural analogues of the unalloyed perovskite BaZrS$_3$. However, we note as a caveat that, given the
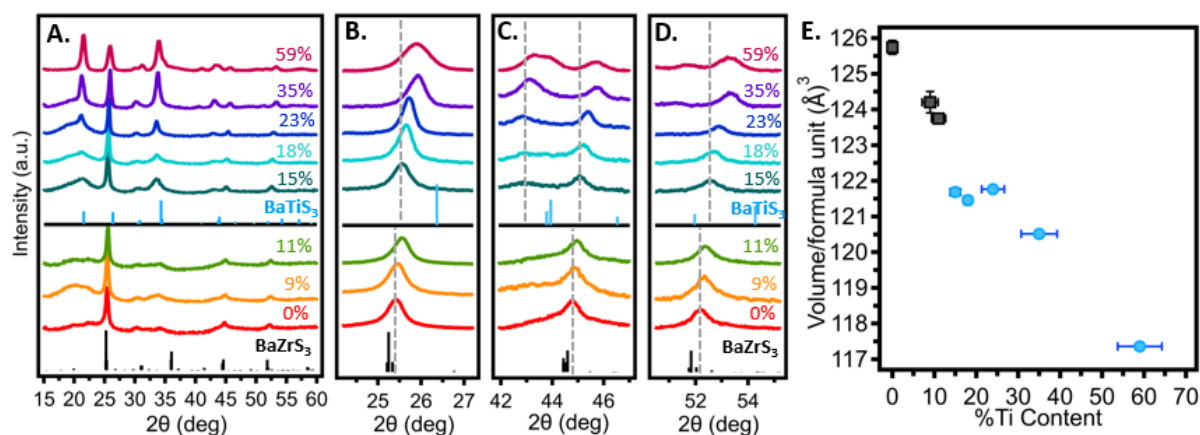

Figure 2. Structural analysis of Ti-alloyed Ba(Zr$_{1-x}$Ti$_x$)S$_3$ nanocrystals and variation in unit cell volume as a function titanium content. (A) PXRD data for Ba(Zr$_{1-x}$Ti$_x$)S$_3$ nanocrystals with different percentage contents of Ti^{4+}, compared to the reference structure reported for BaZrS$_3$ in orthorhombic distorted perovskite (*Pnma*) and BaTiS$_3$ in hexagonal phase (*P*6$_3$/*mmc*). Note that the broad feature around 20° in most samples corresponds to scattering from amorphous components of the sample including excess ligands.[29,57] (B-D) Magnified views of the PXRD data. Vertical dotted lines are guides to the eye to help visualize peak shifts. (E) Volume per formula unit, derived from LeBail fitting of the PXRD data, as a function of measured titanium content (ICP-MS).

limitations of the data, it is difficult to rule out that some samples could be a mixture of phases, e.g. with a portion of a hexagonal-phase alloy as a minor component

In contrast, for $Ba(Zr_{1-x}Ti_x)S_3$ with 15% titanium alloying and higher, the diffraction peaks are more consistent with the predicted pattern of $BaTiS_3$ with the $BaNiO_3$ structural type ($P6_3/mmc$).[24] Notably, as the titanium doping level increases past 11%, new diffraction peaks emerge at 21.5° and 34.3°, associated with the (101) and (201) planes in the $BaNiO_3$ structure type (see Figure S2 for labeled peaks). A magnified view in Figure 2B-D of the PXRD pattern in the regions of three characteristic peaks reveal a generally systematic shift of three diffraction peaks towards higher angles with increasing titanium content; the peak positions tend towards but do not yet reach the expected positions for unalloyed $BaTiS_3$. The analysis of the d-spacing and unit cell parameters as they relate to titanium content is complicated by the fact that, as discussed above, sample-to-sample variation in the lattice cell parameters is expected due to small variations in the sulfur stoichiometry, which may account for deviations from the expected trend in some instances. This is consistent with the fact that the fitted value of the c lattice parameter (which is more strongly affected by these variations) does not cleanly vary systematically with x, while the values of a and the volume per formula unit both show a generally decreasing trend (Figure 2E and Figure S11). Despite this complication, the overall trend, especially as it relates to the decrease in volume per formula unit as the titanium content increases, is clear and remains consistent with successful alloying.

Compositional Analysis

The standard reaction conditions for our nanocrystal synthesis involve a slight excess of the B-site metal cations (zirconium and titanium); since excess B-site cations are removed during the washing process, the Ti^{4+} content in the isolated samples does not necessarily correspond exactly to the nominal amount added to the reaction mixture. The actual elemental compositions of the $Ba(Zr_{1-x}Ti_x)S_3$ samples were determined by ICP-MS (Figure 3). As the amount of titanium precursor added to the reaction mixture was increased, a corresponding systematic increase in the measured titanium content is
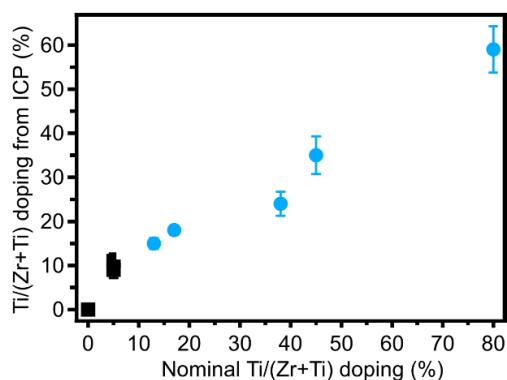

Figure 3. Variation of measured Ti^{4+} content as a function of the nominal titanium content. The black closed squares correspond to samples assigned to the orthorhombic perovskite phase and the blue closed circles correspond to samples in the hexagonal $BaNiO_3$ phase.

observed. Throughout most of the range, the measured titanium content is typically slightly lower than the nominal content (e.g. 80% nominal led to 59% measured titanium), suggesting that there may be slight preference for Zr^{4+} incorporation under our reaction conditions, perhaps due to differing reactivities of the metal precursors or other kinetic or thermodynamic factors related to the growth process. The Ba^{2+} content was also measured by ICP-MS and the Ba:(Zr+Ti) ratios of the $Ba(Zr_{1-x}Ti_x)S_3$ samples are close to the expected stoichiometry. For example, for $x = 0$, $x = 0.09$, and $x = 0.11$, the ratios are 1:1.05, 1:1.0, and 1:1.26, respectively (see Table S2). On average, the B-site cations (zirconium and titanium) were observed by ICP-MS quantification to be slightly in excess relative to barium. It is not uncommon for the overall stoichiometry of small nanocrystals, which are characterized by a high surface-to-volume ratio, to deviate from the theoretical bulk stoichiometry due to surface termination; however, it is difficult to rule out that the apparent excess zirconium and titanium could be due the presence of small amounts of amorphous impurities such as oxides, or due to challenges in completely digesting the samples for ICP analysis.[54,55] To further visualize the distribution of elements within the sample, energy dispersive X-ray spectroscopy (EDX) measurements coupled with TEM imaging were also carried out.

Figure 4 shows the EDX elemental maps for representative $Ba(Zr_{1-x}Ti_x)S_3$ samples with $x = 0$ and $x = 0.23$ (see below for further TEM imaging of these particles; EDX maps for other samples are provided in Figures S12-S13). The elemental mapping reveals a uniform distribution of these elements throughout the doped nanocrystals, indicative of a generally homogeneous composition; the uniform distribution of sulfur co-occurring with the metal ions also suggests that contamination with discrete oxide phases, if any, is relatively minor. The EDX analysis of alloyed samples for the cases with $x = 0$ and $x = 0.23$ revealed percentage compositions of Ba:Zr:Ti:S as 27:19:0:55 and 27:13:4:55, respectively (Table S2). The EDX measurements suggest an excess of barium compared to the total B-site cations; this contrasts with the slightly barium-deficient composition measured by ICP-MS. The precise cause of this discrepancy has not yet been investigated in detail, but could be linked to variations in sample preparation methods between the two elemental analysis techniques (EDX and ICP). It should also be noted that the measured EDX compositions of titanium and barium may be susceptible to inaccuracies due to significant overlap of the barium and titanium characteristic X-ray lines.

Evolution of nanoparticle size and morphology

The morphology of unalloyed $BaZrS_3$ nanocrystals and the alloyed $Ba(Zr_{1-x}Ti_x)S_3$ samples, prepared under standard conditions, was evaluated using transmission electron microscopy (TEM) imaging. Figures 5a-h present TEM images of $Ba(Zr_{1-x}Ti_x)S_3$ samples with values of x ranging from 0 to 0.59, corresponding to the samples whose diffraction patterns were given in Figure 2. Notably, the sample's morphology transforms from nanoplatelets to nanohexagons and ultimately to
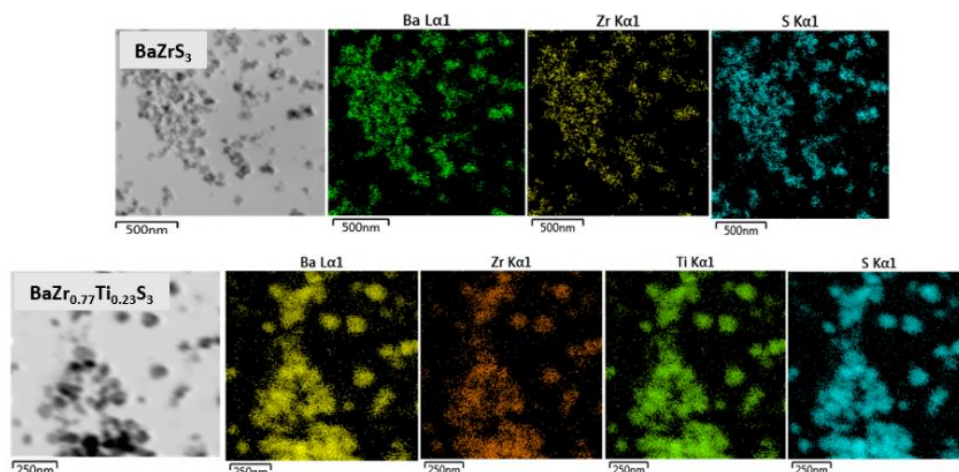
Figure 4. EDX mapping of Ti-alloyed $Ba(Zr_{1-x}Ti_x)S_3$ with (top) x = 0 and (bottom) x = 0.23.

nanobars. Specifically, samples synthesized with low titanium doping levels (x = 0 to 0.15) exhibit nanoplatelet structures (Figures 5a to 5d). At 18% titanium content, the nanocrystals show a much more agglomerated morphology resembling nanoflowers; beyond that (23% titanium), a clear hexagonal morphology begins to take shape (Figures 5e-f). The sample with 35% titanium content is characterized by relatively large and well-defined hexagonal particles (Figure 5g); finally, the highest titanium content sample (59% titanium) transitions to an anisotropic rectangular "nanobar" morphology (Figure 5h). Samples with intermediate compositions (e.g. 44% titanium content, see below) showed a mixture of nanobar and

nanohexagon morphologies. The alterations in nanocrystal morphology are correlated with the observed phase change, and in particular with the emergence of the hexagonal structure at higher titanium content. The presence of lattice fringes, clearly visible in Figure 5g and in higher-resolution images (Figure 6), confirms the high crystallinity of the alloyed nanohexagons. Figure 5i shows the average sizes of the imaged particles as a function of the measured titanium content. At low doping levels (x = 0 to 0.11), the average width of the perovskite-phase nanoplatelets does not change significantly, ranging from 16 ± 4 nm to 18 ± 5 nm. However, during the transition to the hexagonal phase for doping levels of x = 0.15
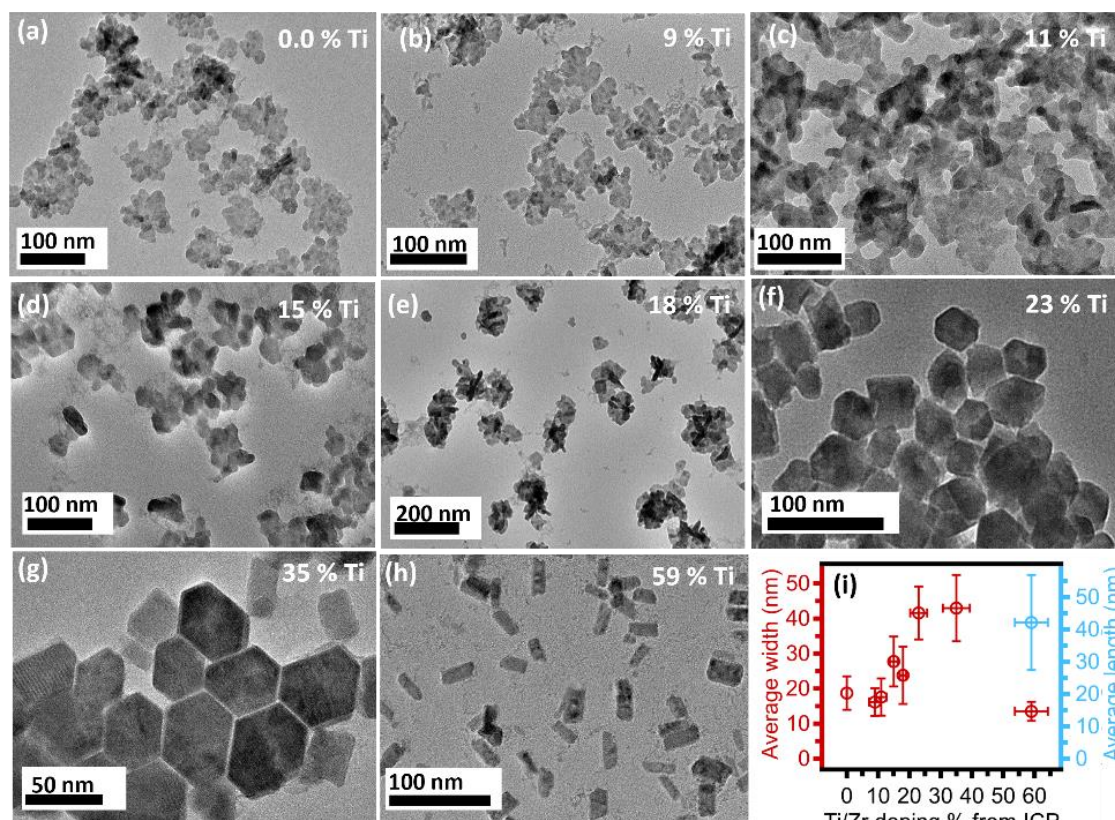

Figure 5. Morphological evolution of Ti-alloyed $Ba(Zr_{1-x}Ti_x)S_3$ viewed using TEM. TEM image of Ti-alloyed $Ba(Zr_{1-x}Ti_x)S_3$ (a) x = 0 (b) x = 0.09 (c) x = 0.11 (d) x = 0.15. (e) x = 0.18 (f) x = 0.23 (g) x = 0.35 (h) x = 0.59 (i) Average size distribution of the Ti-alloyed $Ba(Zr_{1-x}Ti_x)S_3$ nanoparticles.

to 0.35, the average size appears to steadily increase as the nanocrystals take on a more well-defined hexagonal shape, ranging from 24 ± 5 nm to 43 ± 10 nm. For the nanobar particles at higher titanium content, a slight decrease in overall size is observed concomitant with the change in morphology. The observed trends in morphology, especially in the limits of high- and low-titanium content, are consistent with what we have previously reported for $BaZrS_3$ and $BaTiS_3$ nanoparticles— specifically, previously reported $BaZrS_3$ nanoparticles have a rather poorly-defined, aggregated nanoplatelet morphology (Figure 5a) while $BaTiS_3$ nanoparticles tended to have an elongated nanorod morphology, although this was dependent on the reaction conditions.[38,42] Interestingly, well-defined and highly crystalline nanohexagon-like particles of the type observed for $Ba(Ti_{0.35}Zr_{0.65})S_3$ were not observed in the case of unalloyed $BaTiS_3$ under any of the reaction conditions we previously studied.

Figure 6 shows a transmission electron microscopy (TEM) image of $Ba(Zr_{1-x}Ti_x)S_3$ nanoparticles for $x = 0.35$, showcasing lattice fringes, and the fast Fourier transform (FFT) of the image (inset). The analysis of the d-spacing from line profiles of the highlighted regions of the particle (Figure S15) yields values of 0.34 nm and 0.59 nm, which could correspond to the $(1\bar{1}0)$ and $(2\bar{1}0)$ sets of diffraction planes. Additionally, electron diffraction was conducted on a representative $Ba(Zr_{1-x}Ti_x)S_3$ sample ($x = 0.28$), which confirmed the crystallinity and phase of the imaged particles and was consistent with the diffraction pattern observed by PXRD (Figure S14).

Optical properties

The optical band gap of bulk $BaZrS_3$ has been reported in the range of 1.75 to 1.95 eV by different sources; Sopiha *et al.* have suggested that this variation is likely due to a combination of factors potentially including (Urbach) band tailing, the presence of forbidden or partially forbidden transitions at the band gap, and/or the presence of small amounts of impurity phases with lower bandgaps.[12–14,16–21,32] A blue-shifted bandgap of around ~2.3 eV was estimated in a previous report of $BaZrS_3$ nanocrystals by Tauc-type analysis of the optical spectrum, with complementary photoluminescence at 2.08 eV, suggesting the possibility of quantum confinements effects.[39] As discussed
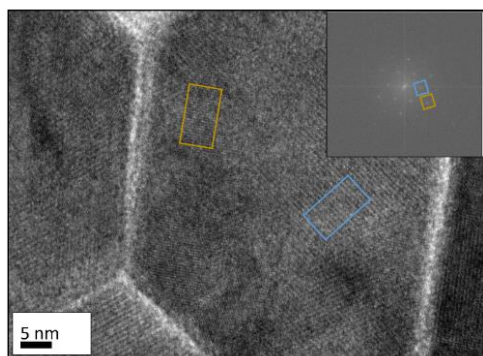
above, alloying with titanium, even at relatively low levels, has been predicted computationally and demonstrated experimentally to have a strong effect on the absorbance spectrum and bandgap, increasing the absorbance at low-energies and lowering the bandgap to the range of 1.51-1.63 eV for 4-5% titanium doping. However, the absorbance spectra for samples at higher titanium alloying levels, including past the phase transition to hexagonal, have not been previously discussed. In general, the pseudo-one dimensional hexagonal-phase ABS_3 compounds have significantly lower bandgaps then the perovskite phases—for $BaTiS_3$ the bandgap lies near 0.3 eV, while the computationally predicted band gap for the hypothetical hexagonal-phase $BaZrS_3$ is approximately 0.4 eV.[15] Nanocrystals of $BaTiS_3$ were observed to have absorbance throughout the NIR region, as expected based on the material's low bandgap, and to exhibit strong absorbance peaks at 1.55 eV and near 0.8 eV.[42]

UV-Vis-NIR extinction spectra of the $Ba(Zr_{1-x}Ti_x)S_3$ nanocrystals as colloids in chloroform are shown in Figure 7, separated into the orthorhombic-phase samples at low x (Figure 7a) and the hexagonal-phase samples at high x (Figure 7b); photographs of the samples are given in Figure S16, showing a gradual change in color from dark brown-red to brown-black. The data are normalized at 500 nm (2.48 eV) to facilitate comparison between different samples. At low titanium content, the perovskite-phase samples show similar sloping absorption spectra (Figure 7a), but the proportion of lower-energy absorption increases as the titanium content increases, and the apparent absorption onset shifts to lower energy. The effect is qualitatively similar to that reported by Wei *et al.* for doping contents of 1-4%.
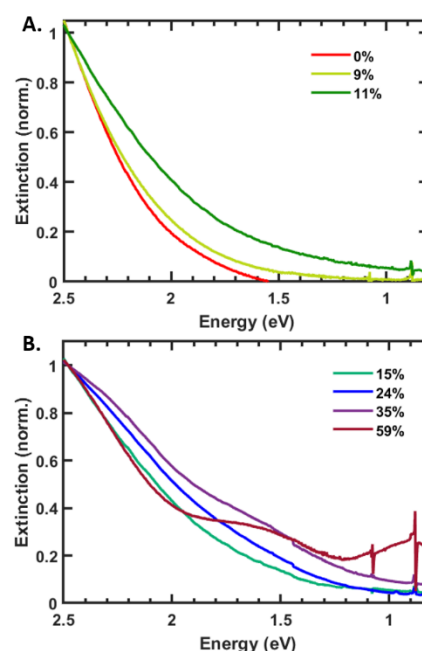

Figure 6. TEM image of $Ba(Zr_{1-x}Ti_x)S_3$ nanoparticles with $x = 0.35$, highlighting regions where lattice fringes are visible. The inset shows the FFT of the TEM image, with spots corresponding to the lattice spacing observed in the highlighted regions indicated.

Figure 7. UV-vis extinction spectra of $Ba(Zr_{1-x}Ti_x)S_3$ nanoparticles, acquired in chloroform. (A) Spectra $BaZr_{1-x}Ti_xS_3$ nanocrystals where $x = 0$ to 0.11, where nanocrystals maintain an orthorhombic perovskite structure. (B) Spectra for hexagonal-phase nanocrystals with $x = 0.15$ to 0.59. Sharp features around 0.9-1.2 eV are related to the solvent background.

As the nanocrystals transition to a primarily hexagonal phase at $x \geq 0.15$, the low-energy absorbance continues to increase and tail into the near-IR. At $x = 0.35$ and $x = 0.59$, features more clearly reminiscent of the $BaTiS_3$ nanocrystal spectra appear, including a peak at 1.55 eV, at essentially the same energy that it appears in the unalloyed $BaTiS_3$ particles. Only at 59% titanium content does the strong near-IR peak previously observed for $BaTiS_3$ nanorods become apparent, here at an energy of 0.93 eV; this energy lies at the upper end of the range over which this peak was observed for the unalloyed particles.[42]

Effect of reaction time and temperature

To further probe the formation of $Ba(Zr_{1-x}Ti_x)S_3$, we explored the influence of temperature and time on the morphology and composition of the particles. Using the standard heat-up reaction conditions, we collected three samples at reaction times of 10, 20, and 30 minutes, starting as the temperature increased from room temperature to 300 °C. The initial 10-minute sample was obtained while the temperature was still rising, at 258 °C; the 20-minute and 30-minute samples were taken after the sample reached the final reaction temperature of 300 °C.

As shown in Figures 8a-c, TEM images reveal a combination of nanoscale hexagons and bars that form within the first 10 minutes of the reaction, with little change in the size and shape of the particles (Figure 8d) over the course of the reaction up through the 30-minute sample. Higher resolution images reveal that well-defined lattice fringes are visible even in the 10 minute-sample, suggesting that highly crystalline particles have already formed (Figure S17). ICP-MS analysis indicated a consistent titanium content of approximately $x = 0.44 \pm 0.1$ in all three samples, suggesting that there are no further significant changes in the metal ion composition after initial formation of the particles. We also tested longer reaction times (1 hour) for several different titanium concentrations, which did not seem to noticeably change the outcome of the reaction in terms of the particle size and composition as measured by
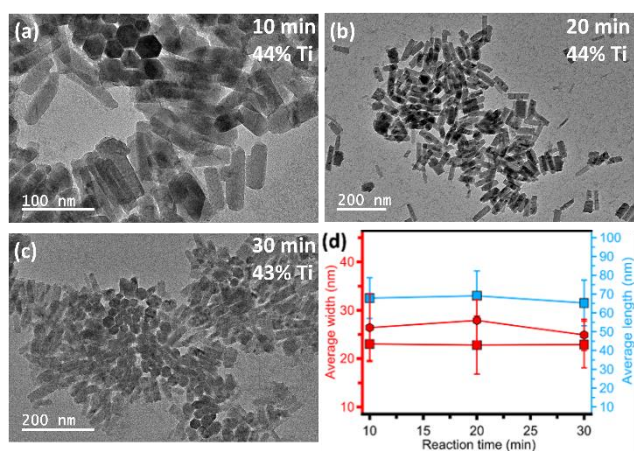
PXRD, but did result in an increased tendency to form crystalline impurities (Figure S18).

Figure 9 shows the PXRD data for the three samples taken from 10 to 30 min of reaction time. An aliquot collected earlier, at 5 minutes of reaction time when the temperature had reached approximately 200 °C, did not exhibit observable crystallinity according to PXRD. However, the diffraction patterns of samples collected at 10 minutes (258 °C) and later at the final reaction temperature (300 °C) were consistent with nanocrystals with the hexagonal $P6_3/mmc$ structure. Slight changes in the diffraction pattern during the course of the reaction mirror what was previously observed in our study of the reaction-time-dependent properties of unalloyed $BaTiS_3$ nanorods.[42] Small shifts in the positions of certain diffraction peaks are evident when comparing samples taken at 20 and 30 minutes to those from the shorter 10-minute reaction at 258°C (Figure 9). Specifically, diffraction peaks corresponding to the (101), (002), and (201) planes exhibit a shift towards higher angles as the reaction progresses and reaches higher temperature. Similar changes have been observed in the solid state; in a study by Saeki et al.,[52] it was observed that raising the reaction temperature from 750 °C to 900 °C caused increased sulfur deficiencies ($BaTiS_{2.93}$–$BaTiS_{2.7}$), which resulted in a shortening in the apparent c-axis periodicity of the structure.

Stability

The superior stability of $BaZrS_3$ under ambient conditions is generally cited as one of its most significant potential advantages relative to the lead halide perovskites, and studies on bulk powders suggest that this stability also extends in part to alloyed $Ba(Zr_{1-x}Ti_x)S_3$ materials. For a $Ba(Zr_{1-x}Ti_x)S_3$ bulk powder prepared with 4% titanium, Wei *et al.* reported that minimal degradation was observed after one hour of annealing under O_2 at 500 °C, or after 890 hours at room temperature under ambient atmosphere, similar to their results for unalloyed $BaZrS_3$; however, upon raising the annealing temperature to 800 °C, significantly more degradation was observed for the alloyed sample than for $BaZrS_3$ itself, although the latter also showed partial degradation.[18] This suggested that the stability of the alloyed material was somewhat compromised even at low levels of titanium incorporation. Therefore, we were interested to test whether a similar effect
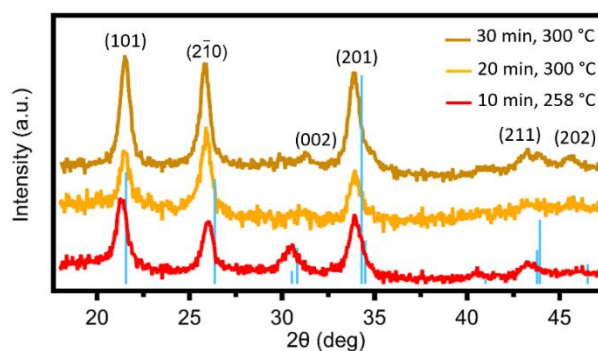

Figure 8. TEM images of $Ba(Zr_{1-x}Ti_x)S_3$ nanocrystals from reaction aliquots taken at (a) 10 minutes at 258 °C (b) 20 minutes at 300 °C (c) 30 minutes at 300 °C. (d) Average size distribution of nanocrystals at each time point.

Figure 9. PXRD data of $Ba(Zr_{1-x}Ti_x)S_3$ aliquot reaction taken at different times during the course of heating from room temperature to 300 °C. The blue lines correspond to a reference pattern calculated for unalloyed $BaTiS_3$.

ARTICLE   **Journal Name**

could be observed in nanocrystals, where atmospheric degradation is often accelerated due to the high surface-to-volume ratio of the particles.

To assess the stability of low and high titanium-alloyed Ba(Zr$_{1-x}$Ti$_x$)S$_3$ nanocrystals, specifically with x values of 0.11 and 0.35, we exposed these two samples to ambient conditions and monitored them using PXRD for up to 8 weeks (Figure 10A-B). In the case of the nanocrystals with 11% titanium alloying, the PXRD data reveals a gradual broadening of peak widths, indicative of partial crystallinity loss, likely due to surface oxidation upon exposure to air. Furthermore, an unidentified peak emerged after 8 weeks, suggesting a possible formation of secondary phases; however, some amount of nanocrystalline Ba(Zr$_{1-x}$Ti$_x$)S$_3$ is still detectable at the end of this time (Figure 10A). The alloyed hexagonal-phase Ba(Zr$_{0.65}$Ti$_{0.35}$)S$_3$ nanocrystals (Figure 10B) showed poor stability under ambient conditions, with no detectable crystalline material remaining after 4 weeks. Consistent with these observations and potential oxide formation, the 11% titanium sample changed in color

from dark brown to pale brown while the 35% sample changed in color from black to off-white.

The stability of Ba(Zr$_{1-x}$Ti$_x$)S$_3$ was also probed using XPS analysis of a sample with 59% titanium content (Figures S19-S20; Tables S3-S6) using aluminum K$_\alpha$ X-rays (1.487 keV). Before aging, the XPS spectra in the Zr 3d, Ba 3d, and S 2p regions are qualitatively similar to XPS data previously reported for bulk and thin-film BaZrS$_3$ collected with the same photon energy.[56–59] The zirconium 3d region shows evidence for a mixture of sulfide species and other impurities that may be due to the presence of some oxidized species even after only brief air exposure (Figure S19), while the sulfur 2p region is dominated by a peak near 160 eV which has been attributed to the sulfide perovskite, while oxidized sulfur impurities (e.g. sulfate) are also evidence by a smaller, broad feature near 167 eV (Figure S19). After two weeks of aging, accompanied by a color change to off-white, the zirconium 3d region is a more complex mixture of overlapping and broadened peaks likely due to the presence of various oxide, hydroxide, sulfate, and similar degraded species (Figure S20). More strikingly, in the sulfur 2p region, the intensity in the sulfide region has disappeared, leaving only some broad signal in the oxidized sulfur region (Figure S20). This data is consistent with nearly complete degradation of this sample over the course of two weeks of air exposure.

Interestingly, this outcome differs from our previously reported stability findings for unalloyed BaZrS$_3$ and BaTiS$_3$ under similar conditions.[38] The unalloyed BaZrS$_3$ showed little to no discernible degradation after 9 weeks in air, compared to significant (albeit incomplete) degradation for the perovskite-phase 11% titanium-doped sample. While unalloyed hexagonal-phase BaTiS$_3$ did show some loss of crystallinity over a similar time period, attributed to surface oxidation, the majority of the sample appeared to persist in the BaTiS$_3$ phase, in contrast to the complete degradation observed here for the hexagonal-phase 35% titanium-containing sample.[42] A close examination of the PXRD data for the 11%-doped sample during the stability study shows a slight shift of the position for the prominent peak near 25.5° over time; in particular, the peak shifts to lower angles over the first six weeks. This would be consistent with a decrease of the titanium content in the nanocrystalline components of the material, perhaps due either to ion migration and extrusion of titanium to the surfaces of the particles, or preferential degradation/amorphization of more titanium-rich areas. The reason for the apparent peak shift back towards higher angles at week 8 is unclear, but perhaps could be related to increasing incorporation of oxygen especially near the surface.

Figure 10. Investigations of the environmental stability of nanocrystals in the Ba(Zr$_{1-x}$Ti$_x$)S$_3$ system. Panels (A) and (B) show PXRD patterns for nanocrystals with x = 0.11 (A) and x = 0.35 (B) upon exposure to ambient atmosphere for up to 8 weeks. The black and blue sticks in (A) and (B) correspond to the calculated reference patterns for BaZrS$_3$ and BaTiS$_3$, respectively. In panel (C), the peak position and peak FWHM are tracked over time for the 11% Ti sample shown in panel (A).

Computational comparison of orthorhombic and hexagonal Ba(Zr$_{1-x}$Ti$_x$)S$_3$ phases

Several prior works have used DFT computations to predict the electronic structure and optical properties of Ba(Zr$_{1-x}$Ti$_x$)S$_3$ alloys; in addition to the original report by Meng *et al.* discussed above, computational work was presented alongside experimental work by Nishigaki *et al.* and Sharma *et al.*; further computational studies were also reported recently by Kanoun
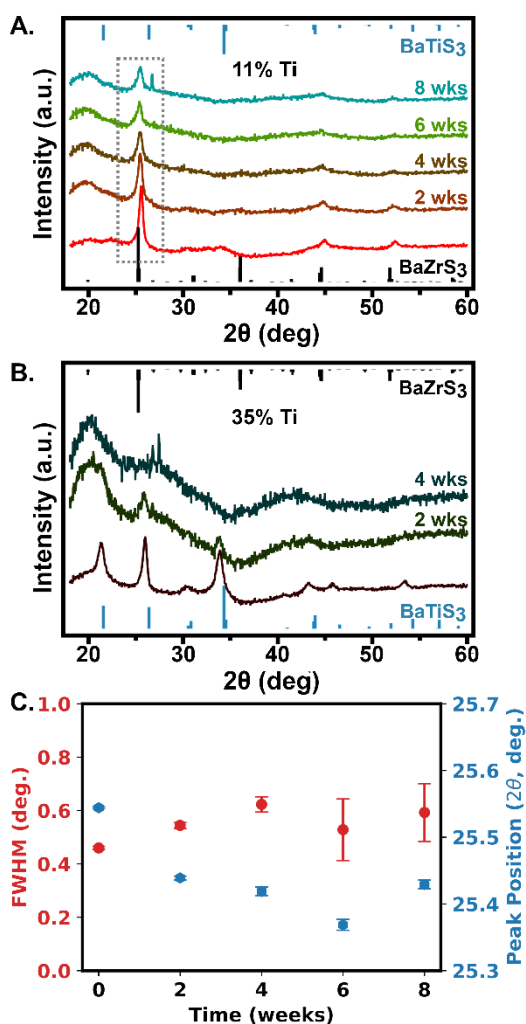
et al., including numerical simulations of solar device performance.[14,19,20,23] Computations on the related material Ba(Hf$_{1-x}$Ti$_x$)S$_3$ by Kong *et al.* also gave rise to similar results about the impact of titanium doping on the perovskite.[60] Despite differences in methodology and small differences in the quantitative results, these DFT studies have had qualitatively similar outcomes, showing a steep drop in band gap upon the incorporation of even low levels of titanium. However, previous computational work has assumed that an orthorhombic perovskite phase is maintained throughout the compositional range, inconsistent with experiment, and has not examined other details such as the effect of the distribution of titanium ions on the electronic structure. We therefore pursued DFT calculations on both the orthorhombic and hexagonal phases to further contextualize our results about the phase preferences of the alloy system and to probe the impact of dopant distribution.

The structures of BaZrS$_3$, BaTiS$_3$, and Ba(Zr$_{1-x}$Ti$_x$)S$_3$ for titanium contents of 6.25%, 12.5%, 25%, and 50% were optimized in both the orthorhombic and hexagonal phases using the reported *Pnma* and *P6$_3$/mmc* crystal structures, respectively, as the starting points. A 2x1x2 supercell was used for the orthorhombic phase and a 2x2x2 supercell for the hexagonal phase, resulting in 16 independent B-site cations in both cases; for alloyed structures, 1, 2, 4, or 8 of the zirconium ions in the B-sites were replaced by titanium. In the cases with more than one titanium ion, multiple possible structures with different arrangements of the dopant ions were considered. The possible structures were generated with the program Supercell and a subset of structures were selected for optimization, specifically including structures with clustered titanium ions, well-separated and ordered titanium ions, and some with a more random distribution.[61] Computational parameters (see Supporting Information) were selected to give good agreement with the experimentally observed crystal structure of BaZrS$_3$ and to converge the calculated energies at reasonable computational cost given the large systems involved.

A comparison of the calculated enthalpy of the orthorhombic and hexagonal phases at each composition is shown in Figure 11a, where the enthalpy relative to the most stable calculated orthorhombic structure is shown; enthalpies are given per mole of the formula unit. Consistent with experiment, the orthorhombic perovskite phase is favored for

the pure BaZrS$_3$ material, while the hexagonal pseudo-one-dimensional phase is favored for the pure BaTiS$_3$ material. There is a nearly linear decrease in the relative energy of the hexagonal Ba(Zr$_{1-x}$Ti$_x$)S$_3$ from $x = 0$ to $x = 1$, with a predicted inversion near 70% Ti. The calculation, therefore, does overestimate the stability of the orthorhombic perovskite phase for intermediate alloyed compositions, given that we observed experimentally a change in phase to hexagonal in the range of 11-15% titanium. Nevertheless, the general trends are consistent experimentally and computationally. There are several possible factors that may contribute to the imperfect agreement, including the fact that the calculations do not capture the true nature of the hexagonal structure as an incommensurate composite lattice,[52] possible differences between nanoscale materials and bulk, the fact that our reactions may occur at least in part under kinetic control rather than being fully thermodynamically controlled, and practical limitations to the accuracy of the DFT calculations. Calculations of the volume per formula unit follow the same trend as those observed experimentally (Figure 11b). Interestingly, in all cases where multiple possible distributions of the alloyed ions were tested, the lowest energy relaxed structure was a relatively high-symmetry structure with the minority ions distributed homogeneously, without any nearest-neighbor pairs, rather than clustered; for the 50% titanium case the lowest-energy structure was characterized by precisely alternating zirconium and titanium ions. The low-energy structures and selected alternate structures are shown below (12.5% titanium, *vide infra*) and in the SI (25% and 50% titanium, Figures S21-S22).

Calculations of the electronic structure using GGA+U methods gave an estimate of the band gap for BaZrS$_3$ in the orthorhombic perovskite phase of 1.64 eV. As is common with DFT-GGA methods, this somewhat underestimates the experimentally determined values which have ranged from ~1.74 eV to 1.94 eV, and is slightly below the value of 1.76 eV determined from calculations at the HSE06 level. However, because of the large size of the systems used for calculating the alloyed systems especially at low titanium content, HSE06 calculations were considered impractical, and the GGA+U methods can reproduce well the trends in the bandgaps as well as the density-of-states and band structures despite the underestimation of the absolute value, as confirmed by prior computational work on chalcogenide perovskite systems.[14] Results in the orthorhombic perovskite phase are generally consistent with those previously reported, marked by a steady decrease in bandgap
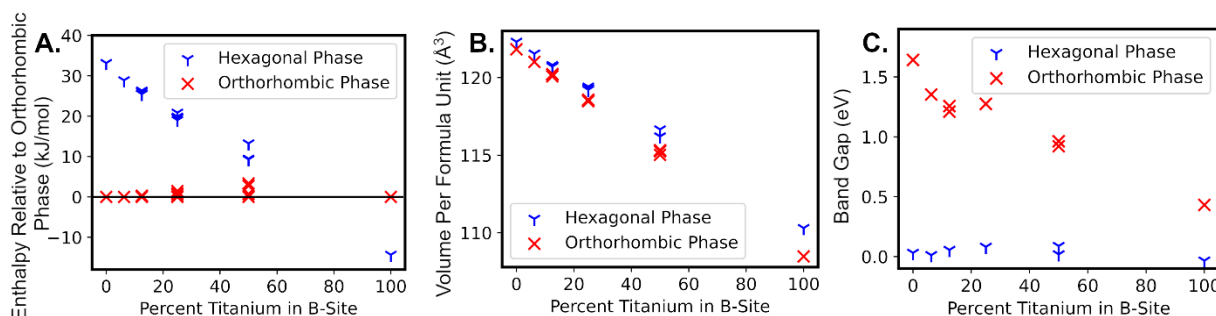

Figure 11. Computationally determined dependence of enthalpy (A), volume per formula unit (B), bandgap (C), and band edge energies (D) on the percent of titanium ions in the B sites. Enthalpy is given per formula unit and relative to the lowest energy calculated structure for a given composition.
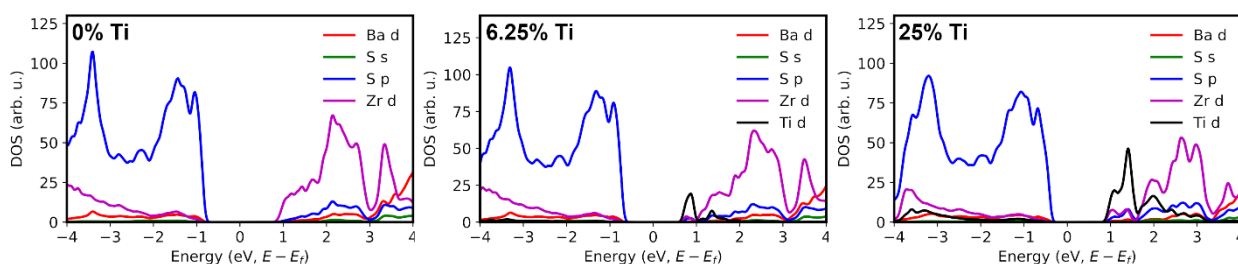
Figure 12. Plots of the calculated partial density of states for selected atomic orbitals for Ba(Zr$_{1-x}$Ti$_x$)S$_3$ in the orthorhombic perovskite phase for different percentage Ti contents. Energies are plotted relative to the Fermi level (E_f), which is set to the middle of the bandgap.

as Ti^{4+} is incorporated into the lattice. We noted an initial particularly sharp drop in the bandgap upon incorporation of the first titanium ion into the calculated system (6.25% doping, Figure 11c); after that, the bandgap continues to decrease as more titanium is incorporated, albeit more gradually.

An examination of the partial density of state (PDOS) plots for some of these compositions helps contextualize these results (Figure 12 and Figures S21-S22). In these materials, the valence band edge is composed largely of sulfur p-states while the conduction band edge is composed primarily of the B-site metal d-states, with some mixing indicative of covalency. Upon incorporation of the fist titanium atom into the supercell, the appearance of a new set of states primarily composed of titanium d-orbitals at the bottom of the conduction band is apparently responsible for the abrupt drop in the calculated band gap. As additional titanium atoms are incorporated, the density of these low-energy conduction band states increases proportionally, although the change in energy is smaller.

Different arrangements of the alloyed B-site ions had a minor effect on the calculated band gaps (Figure 13; Figures S24-S25). For example, when the 12.5% titanium case in an orthorhombic structure is considered, the lowest energy structure (with isolated titainium ions) is only slightly lower in energy (~0.5 kJ/mol) than an alternative arrangement with linearly clustered titanium ions; the bandgap of the latter was lower by approximately 50 meV (Figure

13). Despite the relatively small change, this suggests that inhomogeneities in the titanium dopant distribution likely contribute to the observed band-edge absorption broadening (increased Urbach energy) of the alloys, for instance as described by Nishigaki *et al.* for thin films of Ba(Zr$_{1-x}$Ti$_x$)S$_3$.[20]

Conclusions

Overall, our study successfully demonstrated the solution-phase synthesis of Ba(Zr$_{1-x}$Ti$_x$)S$_3$ colloidal nanoparticles with a controllable titanium content, and the first reported synthesis of these alloyed materials by a method other than oxide sulfurization. Reactive metal amide precursors in oleylamine solvent facilitated the synthesis at temperatures at or below 300 °C. The Ba(Zr$_{1-x}$Ti$_x$)S$_3$ nanoparticles underwent a phase transition from an orthorhombic to a hexagonal structure at titanium concentrations exceeding approximately x = 0.11, accompanied by a morphological shift from nanoplatelets to nanohexagons and nanobars. The optical property analysis revealed a reduction in the absorption onset of Ba(Zr$_{1-x}$Ti$_x$)S$_3$ nanocrystals and increased low-energy absorption, corresponding to a decreased band gap; high-titanium-content nanoparticles in the hexagonal phase exhibited near-IR absorption consistent with a transition to a low band-gap phase. Investigations into reaction time and temperature showed that Ba(Zr$_{1-x}$Ti$_x$)S$_3$ nanocrystals form within the first 10 minutes of the heat-up reaction at temperatures as low as 258 °C. Stability tests indicated that nanocrystals with higher titanium incorporation (x = 0.35) are less stable to ambient atmosphere than those with lower titanium content (x = 0.11), and both are somewhat less stable than the corresponding unalloyed phases. This study provides new potential pathways for the preparation of alloyed chalcogenide perovskite materials and new insights into the properties of group 4 transition metal chalcogenide nanomaterials with diverse compositions.

Figure 13. Changes in the partial density of states (PDOS) and band gap for structures with different Ti^{4+} dopant distributions, shown for the 12.5% Ti^{4+} case in the orthorhombic perovskite structure (corresponding 2 Ti ions out of 8 octahedral B-sites in the calculated supercell). (A) and (B) show the relaxed structure and PDOS plots for the lowest-energy calculated structure while (C) and (D) show the relaxed structure and PDOS plots for an alternative structure, higher in energy by 0.5 kJ/mol BaMS$_3$, with Ti^{4+} ions clustered in a 1D chain.

Conflicts of interest

There are no conflicts to declare.

Data availability

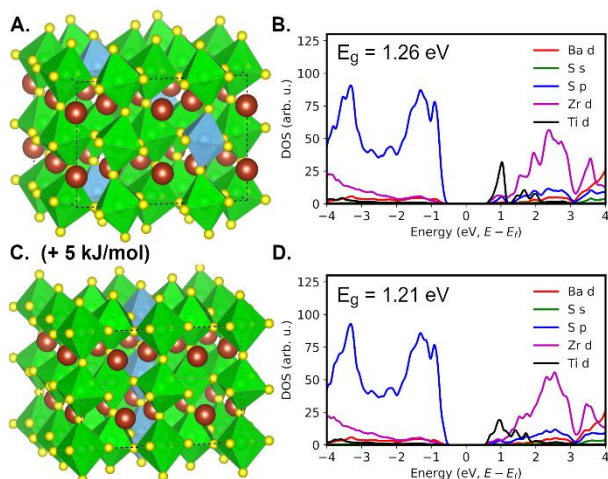Data supporting this article has been included as part of the Supplementary Information.

Acknowledgements

Notes and references

1 H. Zhou, Q. Chen, G. Li, S. Luo, T. Song, H.-S. Duan, Z. Hong, J. You, Y. Liu and Y. Yang, *Science*, 2014, **345**, 542–546.
2 A. Kojima, K. Teshima, Y. Shirai and T. Miyasaka, *J. Am. Chem. Soc.*, 2009, **131**, 6050–6051.
3 M. Liu, M. B. Johnston and H. J. Snaith, *Nature*, 2013, **501**, 395–398.
4 H. Chen, C. Liu, J. Xu, A. Maxwell, W. Zhou, Y. Yang, Q. Zhou, A. S. R. Bati, H. Wan, Z. Wang, L. Zeng, J. Wang, P. Serles, Y. Liu, S. Teale, Y. Liu, M. I. Saidaminov, M. Li, N. Rolston, S. Hoogland, T. Filleter, M. G. Kanatzidis, B. Chen, Z. Ning and E. H. Sargent, *Science*, 2024, **384**, 189–193.
5 P. Zhu, D. Wang, Y. Zhang, Z. Liang, J. Li, J. Zeng, J. Zhang, Y. Xu, S. Wu, Z. Liu, X. Zhou, B. Hu, F. He, L. Zhang, X. Pan, X. Wang, N.-G. Park and B. Xu, *Science*, 2024, **383**, 524–531.
6 G. Li, Z. Su, L. Canil, D. Hughes, M. H. Aldamasy, J. Dagar, S. Trofimov, L. Wang, W. Zuo, J. J. Jerónimo-Rendon, M. M. Byranvand, C. Wang, R. Zhu, Z. Zhang, F. Yang, G. Nasti, B. Naydenov, W. C. Tsoi, Z. Li, X. Gao, Z. Wang, Y. Jia, E. Unger, M. Saliba, M. Li and A. Abate, *Science*, 2023, **379**, 399–403.
7 J.-P. Correa-Baena, M. Saliba, T. Buonassisi, M. Grätzel, A. Abate, W. Tress and A. Hagfeldt, *Science*, 2017, **358**, 739–744.
8 H. Tang, Z. Shen, Y. Shen, G. Yan, Y. Wang, Q. Han and L. Han, *Science*, 2024, **383**, 1236–1240.
9 Y.-H. Lin, Vikram, F. Yang, X.-L. Cao, A. Dasgupta, R. D. J. Oliver, A. M. Ulatowski, M. M. McCarthy, X. Shen, Q. Yuan, M. G. Christoforo, F. S. Y. Yeung, M. B. Johnston, N. K. Noel, L. M. Herz, M. S. Islam and H. J. Snaith, *Science*, 2024, **384**, 767–775.
10 R. Guo, D. Han, W. Chen, L. Dai, K. Ji, Q. Xiong, S. Li, L. K. Reb, M. A. Scheel, S. Pratap, N. Li, S. Yin, T. Xiao, S. Liang, A. L. Oechsle, C. L. Weindl, M. Schwartzkopf, H. Ebert, P. Gao, K. Wang, M. Yuan, N. C. Greenham, S. D. Stranks, S. V. Roth, R. H. Friend and P. Müller-Buschbaum, *Nat. Energy*, 2021, **6**, 977–986.
11 D. Zhang, D. Li, Y. Hu, A. Mei and H. Han, *Commun. Mater.*, 2022, **3**, 1–14.
12 S. J. Adjogri and E. L. Meyer, *Materials*, 2021, **14**, 7857.
13 K. V. Sopiha, C. Comparotto, J. A. Márquez and J. J. Scragg, *Adv. Opt. Mater.*, 2022, **10**, 2101704.
14 W. Meng, B. Saparov, F. Hong, J. Wang, D. B. Mitzi and Y. Yan, *Chem. Mater.*, 2016, **28**, 821–829.

15 Y.-Y. Sun, M. L. Agiorgousis, P. Zhang and S. Zhang, *Nano Lett.*, 2015, **15**, 581–585.
16 T. Gupta, D. Ghoshal, A. Yoshimura, S. Basu, P. K. Chow, A. S. Lakhnot, J. Pandey, J. M. Warrender, H. Efstathiadis, A. Soni, E. Osei-Agyemang, G. Balasubramanian, S. Zhang, S. Shi, T. Lu, V. Meunier and N. Koratkar, *Adv. Funct. Mater.*, 2020, **30**, 2001387.
17 X. Wei, H. Hui, C. Zhao, C. Deng, M. Han, Z. Yu, A. Sheng, P. Roy, A. Chen, J. Lin, D. F. Watson, Y.-Y. Sun, T. Thomay, S. Yang, Q. Jia, S. Zhang and H. Zeng, *Nano Energy*, 2020, **68**, 104317.
18 X. Wei, H. Hui, S. Perera, A. Sheng, D. F. Watson, Y.-Y. Sun, Q. Jia, S. Zhang and H. Zeng, *ACS Omega*, 2020, **5**, 18579–18583.
19 S. Sharma, Z. Ward, K. Bhimani, K. Li, A. Lakhnot, R. Jain, S.-F. Shi, H. Terrones and N. Koratkar, *ACS Appl. Electron. Mater.*, 2021, **3**, 3306–3312.
20 Y. Nishigaki, T. Nagai, M. Nishiwaki, T. Aizawa, M. Kozawa, K. Hanzawa, Y. Kato, H. Sai, H. Hiramatsu, H. Hosono and H. Fujiwara, *Sol. RRL*, 2020, **4**, 1900555.
21 S. Niu, H. Huyan, Y. Liu, M. Yeung, K. Ye, L. Blankemeier, T. Orvis, D. Sarkar, D. J. Singh, R. Kapadia and J. Ravichandran, *Adv. Mater.*, 2017, **29**, 1604733.
22 A. Swarnkar, W. J. Mir, R. Chakraborty, M. Jagadeeswararao, T. Sheikh and A. Nag, *Chem. Mater.*, 2019, **31**, 565–575.
23 M. B. Kanoun, B. Ul Haq, A.-A. Kanoun and S. Goumri-Said, *Energy Fuels*, 2023, **37**, 9548–9556.
24 J. Huster, *Z. Für Naturforschung B*, 1980, **35**, 775–775.
25 R. Yang, J. Nelson, C. Fai, H. A. Yetkin, C. Werner, M. Tervil, A. D. Jess, P. J. Dale and C. J. Hages, *Chem. Mater.*, 2023, **35**, 4743–4750.
26 M. Buffiere, D. S. Dhawale and F. El-Mellouhi, *Energy Technol.*, 2019, **7**, 1900819.
27 K. C. Vincent, S. Agarwal, J. W. Turnley and R. Agrawal, *Adv. Energy Sustain. Res.*, 2023, **4**, 2300010.
28 T. Freund, S. Jamshaid, M. Monavvar and P. Wellmann, *Crystals*, 2024, **14**, 267.
29 M. Surendran, H. Chen, B. Zhao, A. S. Thind, S. Singh, T. Orvis, H. Zhao, J.-K. Han, H. Htoon, M. Kawasaki, R. Mishra and J. Ravichandran, *Chem. Mater.*, 2021, **33**, 7457–7464.
30 C. Comparotto, A. Davydova, T. Ericson, L. Riekehr, M. V. Moro, T. Kubart and J. Scragg, *ACS Appl. Energy Mater.*, 2020, **3**, 2762–2770.
31 C. Comparotto, P. Ström, O. Donzel-Gargand, T. Kubart and J. J. S. Scragg, *ACS Appl. Energy Mater.*, 2022, **5**, 6335–6343.
32 A. A. Pradhan, M. C. Uible, S. Agarwal, J. W. Turnley, S. Khandelwal, J. M. Peterson, D. D. Blach, R. N. Swope, L. Huang, S. C. Bart and R. Agrawal, *Angew. Chem. Int. Ed.*, 2023, **62**, e202301049.
33 J. W. Turnley, K. C. Vincent, A. A. Pradhan, I. Panicker, R. Swope, M. C. Uible, S. C. Bart and R. Agrawal, *J. Am. Chem. Soc.*, 2022, **144**, 18234–18239.
34 H. W. Hillhouse and M. C. Beard, *Curr. Opin. Colloid Interface Sci.*, 2009, **14**, 245–259.
35 J.-H. Choi, H. Wang, S. J. Oh, T. Paik, P. Sung, J. Sung, X. Ye, T. Zhao, B. T. Diroll, C. B. Murray and C. R. Kagan, *Science*, 2016, **352**, 205–208.
36 V. K. Ravi, S. H. Yu, P. K. Rajput, C. Nayak, D. Bhattacharyya, D. S. Chung and A. Nag, *Nanoscale*, 2021, **13**, 1616–1623.
37 D. Zilevu and S. E. Creutz, *Chem. Commun.*, 2023, **59**, 8779–8798.
38 D. Zilevu, O. O. Parks and S. E. Creutz, *Chem. Commun.*, 2022, **58**, 10512–10515.
39 R. Yang, A. D. Jess, C. Fai and C. J. Hages, *J. Am. Chem. Soc.*, 2022, **144**, 15928–15931.
40 M. McQuarrie and F. W. Behnke, *J. Am. Ceram. Soc.*, 1954, **37**, 539–543.

41 B. Okai, K. Takahashi, M. Saeki and J. Yoshimoto, *Mater. Res. Bull.*, 1988, **23**, 1575–1584.

42 D. Zilevu and S. E. Creutz, *Chem. Mater.*, 2021, **33**, 5137–5146.

43 S. Niu, G. Joe, H. Zhao, Y. Zhou, T. Orvis, H. Huyan, J. Salman, K. Mahalingam, B. Urwin, J. Wu, Y. Liu, T. E. Tiwald, S. B. Cronin, B. M. Howe, M. Mecklenburg, R. Haiges, D. J. Singh, H. Wang, M. A. Kats and J. Ravichandran, *Nat. Photonics*, 2018, **12**, 392–396.

44 B. A. Vaartstra, J. C. Huffman, W. E. Streib and K. G. Caulton, *Inorg. Chem.*, 1991, **30**, 121–125.

45 B. H. Toby and R. B. Von Dreele, *J. Appl. Crystallogr.*, 2013, **46**, 544–549.

46 E. B. Segal, *Chem. Health Saf.*, 2000, **7**, 18–23.

47 P. Giannozzi, S. Baroni, N. Bonini, M. Calandra, R. Car, C. Cavazzoni, D. Ceresoli, G. L. Chiarotti, M. Cococcioni, I. Dabo, A. D. Corso, S. de Gironcoli, S. Fabris, G. Fratesi, R. Gebauer, U. Gerstmann, C. Gougoussis, A. Kokalj, M. Lazzeri, L. Martin-Samos, N. Marzari, F. Mauri, R. Mazzarello, S. Paolini, A. Pasquarello, L. Paulatto, C. Sbraccia, S. Scandolo, G. Sclauzero, A. P. Seitsonen, A. Smogunov, P. Umari and R. M. Wentzcovitch, *J. Phys. Condens. Matter*, 2009, **21**, 395502.

48 P. Giannozzi, O. Andreussi, T. Brumme, O. Bunau, M. B. Nardelli, M. Calandra, R. Car, C. Cavazzoni, D. Ceresoli, M. Cococcioni, N. Colonna, I. Carnimeo, A. D. Corso, S. de Gironcoli, P. Delugas, R. A. DiStasio, A. Ferretti, A. Floris, G. Fratesi, G. Fugallo, R. Gebauer, U. Gerstmann, F. Giustino, T. Gorni, J. Jia, M. Kawamura, H.-Y. Ko, A. Kokalj, E. Küçükbenli, M. Lazzeri, M. Marsili, N. Marzari, F. Mauri, N. L. Nguyen, H.-V. Nguyen, A. Otero-de-la-Roza, L. Paulatto, S. Poncé, D. Rocca, R. Sabatini, B. Santra, M. Schlipf, A. P. Seitsonen, A. Smogunov, I. Timrov, T. Thonhauser, P. Umari, N. Vast, X. Wu and S. Baroni, *J. Phys. Condens. Matter*, 2017, **29**, 465901.

49 M. J. van Setten, M. Giantomassi, E. Bousquet, M. J. Verstraete, D. R. Hamann, X. Gonze and G.-M. Rignanese, *Comput. Phys. Commun.*, 2018, **226**, 39–54.

50 F. Jollet, M. Torrent and N. Holzwarth, *Comput. Phys. Commun.*, 2014, **185**, 1246–1254.

51 R. Lelieveld and D. J. W. IJdo, *Acta Crystallogr. B*, 1980, **36**, 2223–2226.

52 M. Saeki, M. Onoda and Y. Yajima, *J. Solid State Chem.*, 1996, **121**, 451–456.

53 A. Clearfield, *Acta Crystallogr.*, 1963, **16**, 135–142.

54 J. Jasieniak and P. Mulvaney, *J. Am. Chem. Soc.*, 2007, **129**, 2841–2848.

55 C. Morrison, H. Sun, Y. Yao, R. A. Loomis and W. E. Buhro, *Chem. Mater.*, 2020, **32**, 1760–1768.

56 S. Mukherjee, S. Riva, C. Comparotto, F. O. L. Johansson, G. J. Man, D. Phuyal, K. A. Simonov, J. Just, K. Klementiev, S. M. Butorin, J. J. S. Scragg and H. Rensmo, *ACS Appl. Energy Mater.*, 2023, **6**, 11642–11653.

57 S. Riva, S. Mukherjee, S. M. Butorin, C. Comparotto, G. Aggarwal, E. Johannesson, M. Abdel-Hafiez, J. Scragg and H. Rensmo, *ACS Appl. Mater. Interfaces*, 2024, **16**, 40210–40221.

58 J. Xu, Y. Fan, W. Tian, L. Ye, Y. Zhang, Y. Tian, Y. Han and Z. Shi, *J. Solid State Chem.*, 2022, **307**, 122872.

59 Y. Han, J. Xu, Y. Liang, X. Chen, M. Jia, J. Zhang, L. Lian, Y. Liu, X. Li and Z. Shi, *Chem. Eng. J.*, 2023, **473**, 145351.

60 S. Kong, H. Dong, Z. Yu, J. Guo, K. Cao, K. Chen, X. Ke, C. Zhou, J. Deng, S. Yang and Y. Zhang, *Ceram. Int.*, 2024, **50**, 10889–10896.

61 K. Okhotnikov, T. Charpentier and S. Cadars, *J. Cheminformatics*, 2016, **8**, 17.

62 T. J. Boerner, S. Deems, T. R. Furlani, S. L. Knuth and J. Towns, in *Practice and Experience in Advanced Research Computing*, Association for Computing Machinery, New York, NY, USA, 2023, pp. 173–176.

Data supporting this article has been included as part of the Supplementary Information.